A 3D Monte Carlo Analysis of the Role of Dyadic Space Geometry in Spark Generation

Xiaoying Koh, Bhuvan Srinivasan, Hwee Seong Ching, and Andre Levchenko
Whitaker Institute for Biomedical Engineering and Department of Biomedical Engineering, The Johns Hopkins University Whiting School of Engineering, Baltimore, Maryland

ABSTRACT In multiple biological systems, vital intracellular signaling processes occur locally in minute periplasmic subspaces often referred to as signaling microdomains. The number of signaling molecules in these microdomains is small enough to render the notion of continuous concentration changes invalid, such that signaling events are better described using stochastic rather than deterministic methods. Of particular interest is the dyadic cleft in the cardiac myocyte, where short-lived, local increases in intracellular Ca^{2+} known as Ca^{2+} sparks regulate excitation-contraction coupling. The geometry of dyadic spaces can alter in disease and development and display significant interspecies variability. We created and studied a 3D Monte Carlo model of the dyadic cleft, specifying the spatial localization of L-type Ca^{2+} channels and ryanodine receptors. Our analysis revealed how reaction specificity and efficiency are regulated by microdomain geometry as well as the physical separation of signaling molecules into functional complexes. The spark amplitude and rise time were found to be highly dependent on the concentration of activated channels per dyadic cleft and on the intermembrane separation, but not very sensitive to other cleft dimensions. The role of L-type Ca^{2+} channel and ryanodine receptor phosphorylation was also examined. We anticipate that this modeling approach may be applied to other systems (e.g., neuronal growth cones and chemotactic cells) to create a general description of stochastic events in Ca^{2+} signaling.

INTRODUCTION

In the past decade, it has become apparent that multiple intracellular signaling processes occur in minute periplasmic subspaces, often referred to as signaling microdomains (1,2). These are membrane-restricted subcellular spaces where vital, local signaling events can take place to regulate cell function. In these small reaction volumes (in the attoliter range) (3–7), the number of reactant molecules corresponding to physiologically relevant concentrations can be exceedingly low. The reaction system thus cannot be accurately described by a continuous, deterministic approach based on reaction-diffusion ''partial differential equations'', since fluctuations around average values become important and stochastic behavior dominates (8). Here, the familiar macroscopic notion of concentration is no longer useful, necessitating the use of stochastic methods to better describe signaling events. One important example of a microdomain where stochastic events are expected to be prominent is the dyadic cleft of the ventricular myocyte. The dyadic cleft spans an estimated 10- to 12-nm gap (3–7,9) between the voltage-gated L-type Ca^{2+} channels (LCCs) on the transverse tubule (TT) membrane, and ryanodine receptors (RyRs) on the sarcoplasmic reticulum (SR). In response to depolarization of the cardiac action potential (AP), Ca^{2+} influx via LCCs traverses the intracellular compartment to trigger Ca^{2+} release from the closely apposed SR via adjacent Ca^{2+}-sensitive RyRs (Fig. 1 *A*). These events can trigger a fundamentally important positive feedback mechanism of amplifying Ca^{2+} signals known as Ca^{2+}-induced Ca^{2+} release (CICR) (10).

Advances in live-cell imaging techniques have resulted in ever increasing insights into the local Ca^{2+} signaling mechanisms that underlie excitation-contraction (EC) coupling. Although it was known that CICR is responsible for the global Ca^{2+} transient that triggers myocyte contraction, the local nature of the EC coupling control mechanism was not clearly revealed until the discovery of Ca^{2+} sparks by Cheng and co-workers (11). Ca^{2+} sparks, also identified as elementary events of Ca^{2+} release, were first discovered in quiescent rat heart cells using confocal microscopy and the fluorescent Ca^{2+} probe fluo-3 (11). They are short-lived, local increases in intracellular Ca^{2+} that may occur spontaneously or in response to excitation. A single-channel LCC current has been found to be sufficient (12) to activate a cluster of several RyRs to form a Ca^{2+} spark, whereas the spatiotemporal summation of Ca^{2+} sparks gives rise to the cellwide phenomenon of the Ca^{2+} transient.

Over the years, there has been mounting evidence that the control of CICR is contingent upon local Ca^{2+} in the immediate vicinity of the channels, rather than whole-cell Ca^{2+} (12–14). In 1992, Stern proposed the local control theory of EC coupling (see, e.g., Greenstein and Winslow (4), Stern (13), and Niggli and Lederer (15)), which asserts that tight regulation of CICR is made possible by the clustering of LCCs and RyRs into discrete units of Ca^{2+}

Submitted May 3, 2005, and accepted for publication December 5, 2005.

Address reprint requests to Andre Levchenko, Whitaker Institute for Biomedical Engineering, Dept. of Biomedical Engineering, The Johns Hopkins University Whiting School of Engineering, 208C Clark Hall, 3400 North Charles St., Baltimore, MD 21218. Tel.: 410-516-5584; Fax: 410-516-6240; E-mail: alev@jhu.edu.

Xiaoying Koh's present address is Massachusetts Institute of Technology, Biological Engineering Division, Cambridge, MA 02139.

0006-3495/06/03/1999/16 $2.00

doi: 10.1529/biophysj.105.065466

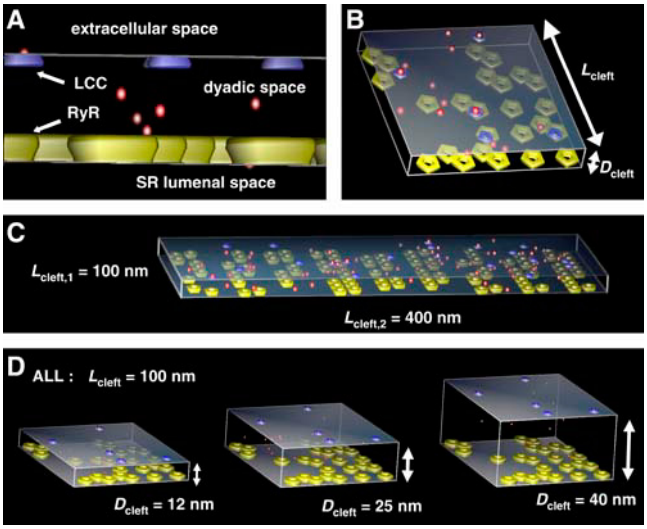

FIGURE 1 Visualization of the model layout and elements. (*A*) Extracellular Ca^{2+} (*red*) enters the dyadic space via LCCs (*blue*) to trigger SR Ca^{2+} release from the Ca^{2+}-sensitive RyRs (*yellow*). (*B*) The standard model cleft is assumed to be a rectangular space where the distance between the TT and SR membranes, denoted as D_{cleft}, is normally 12 nm. The lateral section is square with the *x*,*y* dimensions denoted as L_{cleft}. Bearing in mind the potential variability of cleft geometry, we compare models with fixed numbers of channels and L_{cleft} varying from 100 to 500 nm. Depicted in the figure is the case where L_{cleft} = 100 nm. (*C*) Here, the channel density remains unchanged, whereas the model dimensions are changed. The dimensions are $L_{cleft,1}$ = 100 nm, $L_{cleft,2}$ = 400 nm, and D_{cleft} = 12 nm. (*D*) Models of varying D_{cleft} are compared: 12 nm (*left*), 25 nm (*center*), and 40 nm (*right*). L_{cleft} is fixed at 100 nm. An increase in the average distance between LCCs and RyRs may reduce the triggering of SR Ca^{2+} release.

release, rendering them sensitive to local rather than global Ca^{2+} levels. In other words, macroscopic Ca^{2+} release events are intrinsically controlled by the conductance properties (gating and ion permeation) of individual LCCs and RyRs, and the relative spatial localization of the two channel types. The trigger LCC Ca^{2+} influx has been found to have a tight, smoothly graded control of SR Ca^{2+} release, despite the fact that CICR is a self-regenerative process that intuitively leads to an all-or-none response. This paradox of Ca^{2+} regulation can be explained by the spatial coupling of LCCs and RyRs into functional release units that are able to operate independently, hence providing further evidence for the local control theory. In the rest of this article, we will refer to the site of local control, or the functional Ca^{2+} release unit, as the dyadic cleft (4).

In addition to the type and number of Ca^{2+} channels in the dyadic cleft, the geometry of this functionally significant microdomain is critical to the analysis of Ca^{2+} regulation. The dyadic cleft has been estimated to have a radius of 0.05–0.2 μm, and a height of 10–12 nm (3–7), which gives rise to a volume $\sim 1.0–20.0 \times 10^{-13}$ μL if a cylindrical cleft geometry is assumed. During Ca^{2+} spark formation, the local [Ca^{2+}] in this small compartment may reach a peak of 100 μM to 1 mM during the first 10 ms, and decline rapidly with a halftime of 20 ms to the diastolic [Ca^{2+}] of 1 μM or less (3,6,11,16). These concentration values translate to a maximum of $\sim$1000 ions at peak [Ca^{2+}], and only 1–2 Ca^{2+} ions at rest. Hence, it is clear that at the level of local Ca^{2+} signaling, the number of Ca^{2+} ions can be small enough to render the notion of continuous concentration changes invalid (8). One aspect of cleft geometry that may be a possible feature in failing myocytes is a dramatic phenotypical change in structure, which has been associated with abnormal Ca^{2+} signaling (17–19).

Another important aspect of Ca^{2+} regulation is the possibility that various signaling events can be capable of modulating the properties of molecular species responsible for Ca^{2+} release and uptake. In microdomains like the dyadic cleft, the β-adrenergic receptor (β-AR) signaling complex may be colocalized with immediate downstream effectors into multimolecular complexes for specific signal transduction to Ca^{2+} channels (20,21). Numerous studies have shown a correlation between sustained β-adrenergic stimulation and cardiac dysfunction (22). It is also known that β-adrenergic agonists are able to increase force development and accelerate contractile relaxation by altering channel gating properties. Excessive β-adrenergic stimulation, however, may lead to LCC and RyR hyperphosphorylation, which can impair contractility and cause heart failure (22–24).

In recent years, several computational models incorporating either fully deterministic or partially deterministic methods (3,4,7,25–27) have been developed to explore Ca^{2+} dynamics in the dyadic space. However, Ca^{2+} signaling at the level of individual clefts is highly stochastic and dependent on local Ca^{2+}, suggesting that nondeterministic simulation methods are necessary to achieve a sufficiently detailed description of signaling events.

Here we use a 3D Monte Carlo approach to better describe Ca^{2+} regulation within dyadic clefts of cardiac myocytes. To account for events that involve individual diffusing and reacting molecules, we examined a completely stochastic simulation of localized Ca^{2+} signaling. Simulations are performed with MCell (www.mcell.cnl.salk.edu), a software package designed for realistic simulations of cellular microphysiology. Using this approach, we are able to track the positions of individual molecules on different spatial and temporal scales, as well as predict how specific changes in the physical environment might influence Ca^{2+} signaling. We incorporate, to the largest possible extent, information from available literature into a dyadic cleft model of hypothetical dimensions. Despite extensive studies over the years on Ca^{2+} spark properties, the exact nature and definition of sparks still remain controversial (28,29). Our model is intended to capture the properties of the dyadic cleft as a fundamental site of Ca^{2+} release (9,30–32) by describing in detail the basic elements thought to be necessary for spark formation. In addition, we consider the role of geometry and protein kinase A (PKA)-mediated phosphorylation in Ca^{2+} regulation in the cleft.

METHODS

Structural considerations

The modeled cleft space

Imaging studies in skeletal and cardiac muscles have shown that clusters of RyRs are physically separated on junctional domains of the SR membrane (jSR) (9). It has also been reported that, depending on species, a few tens to up to 200 RyRs are clustered in regular lattice arrays (7). A recent study on channel locations in frog myocytes (33) showed that LCCs also reside in clusters on the sarcolemmal membrane. Moreover, optical experiments examining the distribution of proteins involved in EC coupling indicate that LCCs and RyRs are colocalized into discrete Ca^{2+} release units (CaRU) (34,35). Dissipation of local [Ca^{2+}] from each CaRU takes place so rapidly that it does not normally trigger SR Ca^{2+} release at neighboring junctions. The above findings provide strong evidence for the spatial and functional independence of single dyadic clefts, and support the notion that discretized units of Ca^{2+} release microdomains play a major role in EC coupling. In keeping with these observations, we simulate individual dyadic clefts separately as independent units.

Cleft geometry

For the purposes of our model we assume that the standard cleft is a rectangular space with a square lateral section of x,y dimensions denoted as L_{cleft}, and a z dimension of 12 nm between the TT and SR membranes, denoted as D_{cleft} (Fig. 1 *B*). Ca^{2+} that escapes from the cleft is unlikely to return due to rapid dissipation into the larger surrounding cytosolic space. Hence the cleft sidewalls are regarded as Ca^{2+}-absorbing surfaces, whereas the top and bottom walls are Ca^{2+}-reflecting to account for the impermeability of cell membranes (more on boundary conditions below).

The separation between the SR and exterior membranes may be relatively conserved at 10–12 nm; however, other geometrical properties of clefts differ widely across varying species and muscle types (9). In previous cardiac models, the dyadic cleft has been estimated to span 0.05–0.2 μm in radius and 10–12 nm in height (3–7). However, the complex microarchitecture, more specifically the shape and size of this space, is not explicitly known. Bearing in mind the potential variability of cleft geometry, we compare models with L_{cleft} ranging from 0.1–0.5 μm, and volumes ranging from $1.2–30.0 \times 10^{-13}$ μL. We compare different channel densities by fixing the numbers of channels, and also compare clefts of different dimensions where the channel density remains unchanged (Fig. 1 *C*).

Boundary conditions

Although the dyadic cleft is modeled as a functionally independent unit, it is not isolated in the sense that we do take into account the escape of Ca^{2+} into the surrounding cytosol. MCell maps the positions of surfaces and effector sites (e.g., channel proteins and receptors) in space, and tracks the positions of individual diffusing ligands at every time step. When a ligand is detected at a point of intersection with a surface, there can be different possible outcomes depending on the properties of the surface. For example, at the point of intersection, the surface may be reflective, transparent, absorptive, or occupied by an effector site with an associated chemical reaction mechanism. After entering the dyadic cleft, free Ca^{2+} ions may escape into the neighboring space by diffusion. To account for this escape, the four sidewalls of the rectangular cleft are modified to absorb any Ca^{2+} ions that come into contact. This modification is based on the assumption that the return of Ca^{2+} into the cleft by diffusion is insignificant, since the cleft volume is considerably smaller than the surrounding cytosolic volume. The top and bottom surfaces are modified to reflect Ca^{2+} back into the cleft, to represent the impermeable phospholipid bilayers of the TT and SR membranes, respectively.

The placement of absorptive surfaces at the boundaries of the cleft raised the possibility of a discontinuity in the diffusion gradient along the edges of the cleft. To investigate this effect, large volumes were placed around the cleft, which moved the absorptive surfaces away from the boundaries of the cleft and allowed reentry of Ca^{2+} into the cleft. It was found that the introduction of a pericleft volume to the model did not significantly affect the characteristics of the original Ca^{2+} response (see Supplementary Material). This affirms that the return of Ca^{2+} into the cleft is insignificant and that absorptive boundary conditions can be assumed.

Disruption of TT morphology

There is evidence that TT morphology transforms during myocyte development and heart failure, and that these transformations might be closely linked to observed functional variations in the cell. Instances of such morphology changes in pathologic conditions include abnormally shaped TTs in hypertrophic human heart (17), and TT damage or loss in canine tachycardia-dilated cardiomyopathy (18).

TTs are composed of interconnected elements resembling caveolae (19), which are infoldings of the surface membrane in cells lacking TTs (e.g., atrial cells and neonatal cardiomyocytes). In a study on Ca^{2+} sparks produced in caveolae (36), it was proposed that a 20- to 50-nm increase in the distance between the membranes on which LCCs and RyRs reside might produce sparks with altered spatiotemporal characteristics.

When Wang et al. applied a GΩ-seal patch-clamp on the TT membrane, the efficacy of CICR was observed to be greatly reduced, most likely due to a significant degree of LCC/RyR uncoupling caused by membrane deformation associated with the GΩ-seal (37). This anomalous phenomenon was not observed when a loose MΩ-seal patch-clamp was applied instead. Studies involving aligned and nonaligned myocytes have also associated changes in myocyte morphology with altered channel properties (38), possibly due to the disrupted spatial relationship between channels.

The observations described above point toward the likelihood that disruption of the dyadic cleft geometry, including D_{cleft}, can interfere with the tight local control between LCCs and RyRs, and lead to pathological alterations in Ca^{2+} signaling. A spatial change in LCC/RyR organization in failing hearts may adversely affect the triggering of SR Ca^{2+} release by LCC Ca^{2+} influx (39). This spatial change is often associated with an increase in the average distance between LCCs and RyRs (40). Although the structure of our model does not closely replicate the 3D microarchitecture of a dyadic cleft, we are able to take advantage of its simplicity to make predictions about the effects of altering D_{cleft}. We first observe the Ca^{2+} release events that take place in a model with a normal D_{cleft} of 12 nm. We then observe the effects of changing D_{cleft} systematically to small (9 nm) or large (up to 40 nm) values existing outside the physiological range believed to be possible (Fig. 1 *D*).

Model formulation

Channel stoichiometry

Due to the numerous unknowns in the system we are modeling, it is challenging, if not impossible, to create a model that can reproduce physiological events with absolute accuracy. Next we describe the experimental data serving as the basis for some of the assumptions we make.

When modeling the dyadic cleft, one should keep in mind that the reported densities of Ca^{2+} channel proteins are often ambiguous since they are dependent on the intrinsic architecture of the clefts and may also vary between different species (41) and muscle types. In an ultrastructural study on rat ventricular myocytes (42), the densities of LCCs and RyRs are reported to be 84/μm^2 and 765/μm^2, respectively. In the body muscles of arthropods, the density of RyRs has been estimated to be 1275–1890/μm^2 (41), which translates to 15–28 RyRs residing on a square patch of jSR membrane area of L_{cleft} ~0.1–0.15 μm (CaRUs in the body muscles of arthropods and the skeletal and cardiac muscles of vertebrates have been found to have similar architectures (41)). In specifying the number of channels in each cleft, we consider the above-mentioned data on channel densities, as well as the likely stoichiometry of LCC/RyR coupling. It was

reported that a single LCC is able to trigger the opening of four to six RyRs to generate a spark (37), using a patch-clamp method in conjunction with confocal microscopy. In most simulations described below, a hypothetical dyadic cleft of variable L_{cleft} is composed of five LCCs and 25 RyRs.

LCC gating and permeation

There have been extensive studies in recent years that analyze and characterize single LCC properties in healthy heart cells, and also under a range of conditions that might indicate an increased susceptibility to disease (23,43). We model the stochastic gating of LCCs by specifying unimolecular transitions between adjacent open and closed states. MCell calculates reaction transition probabilities according to user-specified rate constants and determines which transitions will occur per time step. Rate constants (units s^{-1}) for LCC gating are derived from a study on single LCC availability and open probability (P_o) in healthy and failing human ventricles (43) (Table 1).

Cytosolic [Ca^{2+}] (~100 nM) is 10,000 times lower than that in both the SR and extracellular space (~1 mM) (6), creating a strong electrochemical gradient for the passage of Ca^{2+} ions into the dyadic space when Ca^{2+} channels are open. A faithful representation of this gradient across the TT and SR membranes will require the introduction of correspondingly large amounts of Ca^{2+} outside the modeled cleft. Some approximations of SR and extracellular volumes will also have to be made to reproduce the conditions that create a driving force for Ca^{2+} entry. This approach is not feasible in reality because of the required computational time and expense. Instead, we seek to simulate permeation as a quantifiable generation of Ca^{2+} ions that flow from effector-site (channel) locations into the cleft. This is done by expressing unitary Ca^{2+} current (i_{LCC}, units pA) in terms of the rate of Ca^{2+} entry (units s^{-1}).

For each channel, only one reaction event (e.g., single ion entry and channel gating) may occur per Monte Carlo decision time step. Although the channel is in an open state, Ca^{2+} influx takes place via transitions of the open state back to itself (Fig. 2, *A–D*), according to a unimolecular transition probability that is calculated from the specified rate of ion generation. Unitary current can be modeled with reasonable accuracy if the simulation time step is sufficiently small. For example, 1.3 pA of current is equivalent to the entry of four divalent ions per μs, or one ion per 0.25 μs. This implies that a time step of 0.25 μs is small enough to simulate any current not exceeding 1.3 pA. For the purposes of our model, we use a 0.25-μs time step throughout all simulations. This time step has been shown to be sufficiently small, as demonstrated by additional studies in which a range of smaller time steps (up to 10 times smaller at 0.025 μs) were used (see Supplementary Material).

Single LCCs from intact rat ventricular myocytes clamped at 0 mV have been found to elicit inward i_{LCC} ~−0.3 pA (37), which translates to ion generation at a rate of ~10^6 s^{-1} (Table 1). In the model, LCC channel gating is described by transitions between a single closed and open state. Fig. 2 *A* shows the detailed state diagram for the LCC. The kinetics of all LCC reaction mechanisms (gating, permeation, and inactivation) are based on experimentally-derived parameters (37,44,45,43) presented in Table 1. The kinetics presented in the schemes is further explained below.

Inactivation of LCC currents

The inactivation of LCC currents serves as a way to constrain trigger Ca^{2+} influx during the cardiac AP and allows the EC coupling system to return to basal conditions during diastole. It is controlled by processes dependent on membrane potential and intracellular Ca^{2+} (46,47,44), known as voltage inactivation and Ca^{2+} inactivation, respectively. When the LCC is held persistently at a depolarized membrane potential, it can enter and stay in the voltage-inactivated state until membrane repolarization is introduced. In this model, the LCC is able to probabilistically enter a voltage-inactivated state from every reaction state (Fig. 2 *A*), governed by a rate constant derived from experimental findings (44) (see Table 1).

Ca^{2+} inactivation is a negative feedback mechanism triggered by elevated levels of intracellular Ca^{2+}. It has been established that calmodulin (CaM), which is constitutively tethered to the LCC complex, is the Ca^{2+} sensor for this mode of inactivation (48). Results from the same study also suggest that Ca^{2+}-dependent inactivation is contingent on the binding of two Ca^{2+} ions to each of the high-affinity sites of CaM, after which the Ca^{2+}/CaM complex undergoes a conformational change that leads to channel inactivation. The LCC remains in this nonconducting state until the inactivation process is

TABLE 1 L-type Ca^{2+} channel parameters

State transitions	Rate constants	Source
Unitary conductance		
O1 ↔ O1	1×10^6 s^{-1}	Wang et al. (37)
O2 ↔ O2	(i_{LCC} ~0.3 pA)	0mV, 23–25°C, rat ventricular myocyte.
Ca^{2+}-inactivation		
C1 → C2 → Ca^{2+}-inact.	2.3×10^6 M^{-1} s^{-1}	Johnson et al. (45)
O1 → O2 → Ca^{2+}-inact.	2.4 s^{-1}	10°C, bovine brain.
Recovery from inactivation		
Ca^{2+}-inact. → C2 → C1		
Ca^{2+}-inact. → O2 → O1		
Voltage-inactivation		
All → Voltage-inact.	3.15 s^{-1}	Findlay et al. (44) +10 mV, 23°C, guinea pig ventricular myocyte
Gating		
Nonphosphorylated		
O1 → C1	$\tau_{open} = 0.50$ ms	
O2 → C2	$k_{o\to c} = 2000$ s^{-1}	Schröder et al. (43)
C1 → O1	$\tau_{closed} = 21.8$ ms	+20 mV, 21–23°C, human ventricles (nonfailing and failing)
C2 → O2	$k_{c\to o} = 45.87$ s^{-1}	
Phosphorylated		
O1 → C1	$\tau_{open} = 0.69$ ms	
O2 → C2	$k_{o\to c} = 1449$ s^{-1}	
C1 → O1	$\tau_{closed} = 13.7$ ms	
C2 → O2	$k_{c\to o} = 72.99$ s^{-1}	

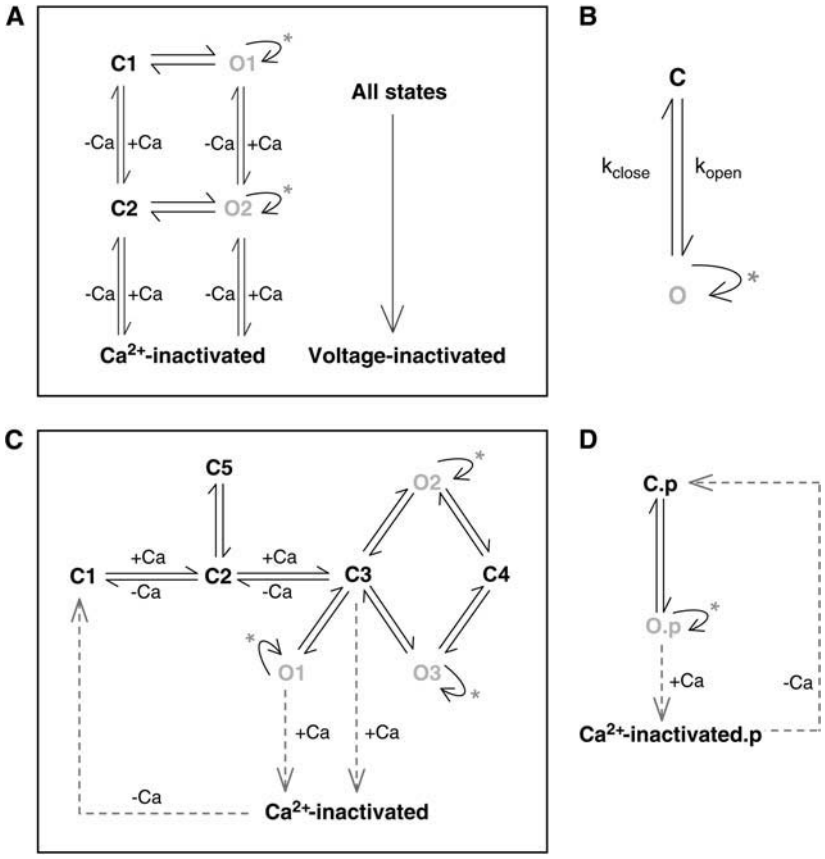

FIGURE 2 Complete state diagrams for the LCC (*A*) and RyR (*C* and *D*). These models incorporate a common schematic for channel gating and permeation that is summarized in panel *B*. The generation of Ca^{2+} (indicated by *asterisks*) is facilitated by open-state (*O*) transitions back to themselves according to a probability of unimolecular transition. (*A*) The LCC enters a Ca^{2+}-inactivated state after two Ca^{2+}-binding events associated with high-affinity CaM sites, whereas recovery from Ca^{2+} inactivation is governed by dissociation of Ca^{2+} from the CaM/LCC complex. Voltage inactivation may proceed from any of the LCC-residing states, and is assumed to be irreversible during the simulation of 250-ms duration. Both nonphosphorylated and phosphorylated LCC models follow the scheme depicted in panel *A*, but use different reaction parameters that were obtained from Schröder et al. (43) (see Table 1). (*C*) The nonphosphorylated RyR model is adopted from a Markovian model described by Saftenku et al. (49), where we also obtained the parameters associated with the closed states C1–C5, and the open states O1–O3. The implementation of RyR Ca^{2+}-dependent inactivation is depicted by dotted lines, and proceeds upon Ca^{2+} binding to handpicked states (*O1*, *C3*) found to be prevalent throughout the simulations. (*D*) We introduce a new model for the phosphorylated RyR (see Methods), which is similar in principle to that depicted in Fig. 2 *B*, with the addition of a Ca^{2+}-dependent inactivation process. Parameters are obtained from a study by Uehara et al. (23) on gating kinetics of phosphorylated RyR (see Table 2).

reversed in the event of a decrease in intracellular Ca^{2+} level. The Ca^{2+}-binding and unbinding events leading to and from Ca^{2+} inactivation are reflected in the detailed model schematic (Fig. 2 *A;* (45)).

RyR state diagram

Saftenku et al. have assessed and described the gating behavior of single cardiac RyRs, using maximum likelihood analysis to estimate single-channel kinetic parameters from experimentally observed dwell times (49). Based on their studies (49), we adopt a Markovian model of the cardiac RyR that reportedly ranked highest among the others, according to the Schwartz criterion. The adopted schematic accounts for activation of the RyR by Ca^{2+}, as well as channel gating between adjacent closed and open states. To complete the description of RyR activity, we append an additional reaction state that represents Ca^{2+}-dependent inactivation (Fig. 2 *C*).

RyR permeation

We incorporate a unitary RyR current (i_{RyR}) of ~0.1 pA, equivalent to an ion generation rate $\sim 0.35 \times 10^6\ s^{-1}$. As is the case for LCC unitary current, this value for i_{RyR} falls within the range of ion generation that may be accurately represented using a 0.25-μs time step. It has been reported that physiological unitary RyR current should be <0.6 pA (50), and possibly as little as 0.07 pA (16). The unitary current value we use corresponds to that from the formulation of an earlier cardiac model (4), where the concentration-dependent SR release flux through single RyRs can be approximated to give rise to unitary currents of ~0.09–0.15 pA during a cardiac cycle.

Termination of SR Ca^{2+} release

Intuitively, CICR seems to be a self-regenerating process operating on the positive feedback of SR release Ca^{2+}. This scenario implies the possibility of unstable global Ca^{2+} oscillations, which we know is not the case in healthy myocytes. A negative control mechanism must exist to terminate the Ca^{2+} spark by interrupting SR Ca^{2+} release. In 1985, Fabiato first proposed a Ca^{2+}-dependent, negative feedback process of CICR inactivation (10). In later years, other mechanisms were proposed, and there has been a growing consensus that the negative control mechanism is actually a composite of processes acting in concert to terminate Ca^{2+} release through the RyRs (7,53). The different hypotheses include (we refer to reviews in (51,52)):

1. Ca^{2+}-dependent inactivation. Experiments have shown that RyRs in cardiac cells are sensitive to jSR Ca^{2+}, and turn off after free [Ca^{2+}] reach high levels.
2. Stochastic attrition. All the RyRs in a release unit have the inherent quality of closing randomly. This process is sensitive to the number of channels in a cluster (13).
3. Adaptation.
4. Depletion of jSR or lumenal [Ca^{2+}].
5. Time-dependent RyR inactivation.

The exact negative control mechanism is still a matter of debate. We choose to model Ca^{2+}-dependent inactivation as a likely mechanism for the termination of SR Ca^{2+} release. Ca^{2+}-dependent inactivation is incorporated into the RyR gating scheme by introducing state transitions into an inactivated state as mediated by Ca^{2+} binding (Table 2 and Fig. 2 *C*) (53). Such transitions are able to proceed from hand-picked states (*O1*, *C3*) found to be prevalent in the scheme. Once inactivated, the RyR is able to recover and return to the basal state via Ca^{2+} dissociation. In a parameter sensitivity study shown in Supplementary Material, we find the range of rates for RyR recovery from inactivation under which the system can display stable behavior. Should RyR recovery happen too readily, there is a possibility that premature sparks can occur before the onset of the next AP. This implies a deregulation of the EC coupling mechanism and a possible trigger of

TABLE 2 Ryanodine receptor parameters

State transitions	Rate constants	Source
Unitary conductance		
O1 ↔ O1	0.35×10^6 s^{-1} (i_{RyR} ~0.1 pA)	Based on:
O2 ↔ O2	<0.07 pA, under physiological conditions	Guatimosim et al. (16)
O3 ↔ O3	<0.6 pA, with competing ions Cs^+ and Mg^{2+}	Mejia-Alaverez et al. (50)
O.p ↔ O.p		
Ca^{2+}-dependent inactivation		
C3, O1 → Ca^{2+}-inact.	9.58×10^4 M^{-1} s^{-1}	Stern et al. (7)
O.p → Ca^{2+}-inact.p		
Recovery from inactivation		
Ca^{2+}-inact. → C1	0.2 s^{-1}	Derived from sensitivity studies (see Results and Supplementary Material)
Ca^{2+}-inact.p → C.p		
Gating		
Nonphosphorylated		
Gating scheme obtained from a Markovian model of cardiac RyRs	Maximum likelihood estimation of rate constants to model RyR gating	Saftenku et al. (49)
Phosphorylated		
O.p → C.p	$\tau_{open} = 2.01$ ms	Uehara et al. (23)
C.p → O.p	$k_{o\to c} = 497.5$ s^{-1}	
	$\tau_{closed} = 1.15$ ms	
	$k_{c\to o} = 869.6$ s^{-1}	

arrhythmic events. Although the addition of the Ca^{2+}-inactivated state provides a pathway that was not present in the original model of Saftenku et al. (49), we find this modification necessary to appropriately describe pertinent properties, in particular the decline of elementary Ca^{2+}-release events.

Effects of β-adrenergic stimulation

β-Adrenergic stimulation of cardiac myocytes has been found to result in a significant increase in both LCC and RyR Ca^{2+} influx, through a process involving channel phosphorylation mediated by the cAMP/PKA pathway (20,22,54). Under the effects of β-adrenergic stimulation, active single-channel sweeps have shown that the increase in Ca^{2+} influx arises from a combined effect of elevated levels of open probability and availability, and is less likely to be a result of elevated unitary current values (23,43).

In this part of our study, we analyze the role of β-adrenergic stimulation in Ca^{2+} signaling by introducing reaction schemes and parameters (Fig. 2, *A* and *D*, and Tables 1 and 2) relevant to channels under phosphorylated conditions. We simulate cases where the cleft molecular stoichiometry remains the same (five LCCs and 25 RyRs) while individual channels are either phosphorylated or nonphosphorylated, as specified. For example, suppose that persistent β-adrenergic stimulation of the myocyte gives rise to phosphorylation of ~20% of the channels. This implies that one LCC and five RyRs in the cleft will be represented by reaction schemes relevant to the phosphorylated case, whereas the other four LCCs and 20 RyRs will be governed by models for nonphosphorylated channels. Our ultimate goal is to describe the impact of channel phosphorylation on Ca^{2+} signaling. Consequently, we do not distinguish between the various β-adrenergic receptor subtypes.

Gating of phosphorylated RyRs is a complex and controversial process that is yet to be fully understood. In the absence of consensus about the exact dynamics of phosphorylated RyRs, we consider a simple model to describe the activity of phosphorylated RyRs. Rather than making modifications to the model in Saftenku et al., which we use to describe nonphosphorylated RyRs, we choose to introduce a new reaction scheme (Fig. 2 *D*) similar in principle to that of the LCC. The phosphorylated RyR gates from a closed state (*C.p*) into an open state (*O.p*), whereas Ca^{2+} generation is mediated by transitions of the open state back to itself. We adopt reaction parameters (Table 2) from values reported in a study by Uehara et al. on the ligand-induced gating kinetics of phosphorylated RyR channels from canine myocytes (23). To describe the termination of SR Ca^{2+} release, we append a Ca^{2+}-dependent inactivated state to the model (Fig. 2 *D*). Since we do not know how phosphorylation may alter the Ca^{2+} sensitivity of RyRs, we begin the phosphorylated RyR in an already-activated state. Studies by Reiken et al. (22) have correlated progressive PKA phosphorylation of RyR to cardiac dysfunction. We want this model to capture interesting effects of phosphorylation that may present a potential indicator for heart disease. We bear in mind that we have made major approximations in this part of our study, such that this set of results may broadly describe effects of phosphorylation but will not reveal other intricate Ca^{2+}-release properties in all accuracy.

Interestingly, the enhanced activity of phosphorylated LCCs bears close resemblance to the behavior of LCCs in failing human ventricular myocytes (43), drawing attention to the idea that a high, steady-state level of LCC phosphorylation is an important feature in heart failure. For the phosphorylated LCC model, we use a scheme similar to that for nonphosphorylated LCCs (Fig. 2 *A*), but change the gating parameters (Table 1) to those obtained from failing hearts. Gating parameters for nonphosphorylated and phosphorylated LCCs are derived from the same experimental study by Schröder et al. (43).

Effects of Ca^{2+} buffering

The association and dissociation of free Ca^{2+} ions with endogenous Ca^{2+} buffers can be one of the determinants of Ca^{2+} spark properties. The majority of these buffers are immobile intracellular molecules with the potential to immobilize Ca^{2+} and momentarily dampen the effects of localized Ca^{2+} elevation. It has been estimated that >90% of Ca^{2+} ions entering a subcellular microdomain are able to bind rapidly to a range of immobile endogenous buffers constituting a variety of Ca^{2+}-binding properties. For example, calmodulin and troponin C possess specific Ca^{2+}-binding sites, whereas the TT and SR phospholipid membranes inherently possess high Ca^{2+}-binding capacity but with low affinity (55).

To examine the effects of buffering on the local Ca^{2+} response, we model a few scenarios of buffering by incorporating immobile, membrane-bound Ca^{2+}-binding sites on the top and bottom surfaces (TT and SR membranes). We compare the consequences of high and low densities of buffers and of buffers with high and low binding affinities, based on previously studied parameters (55).

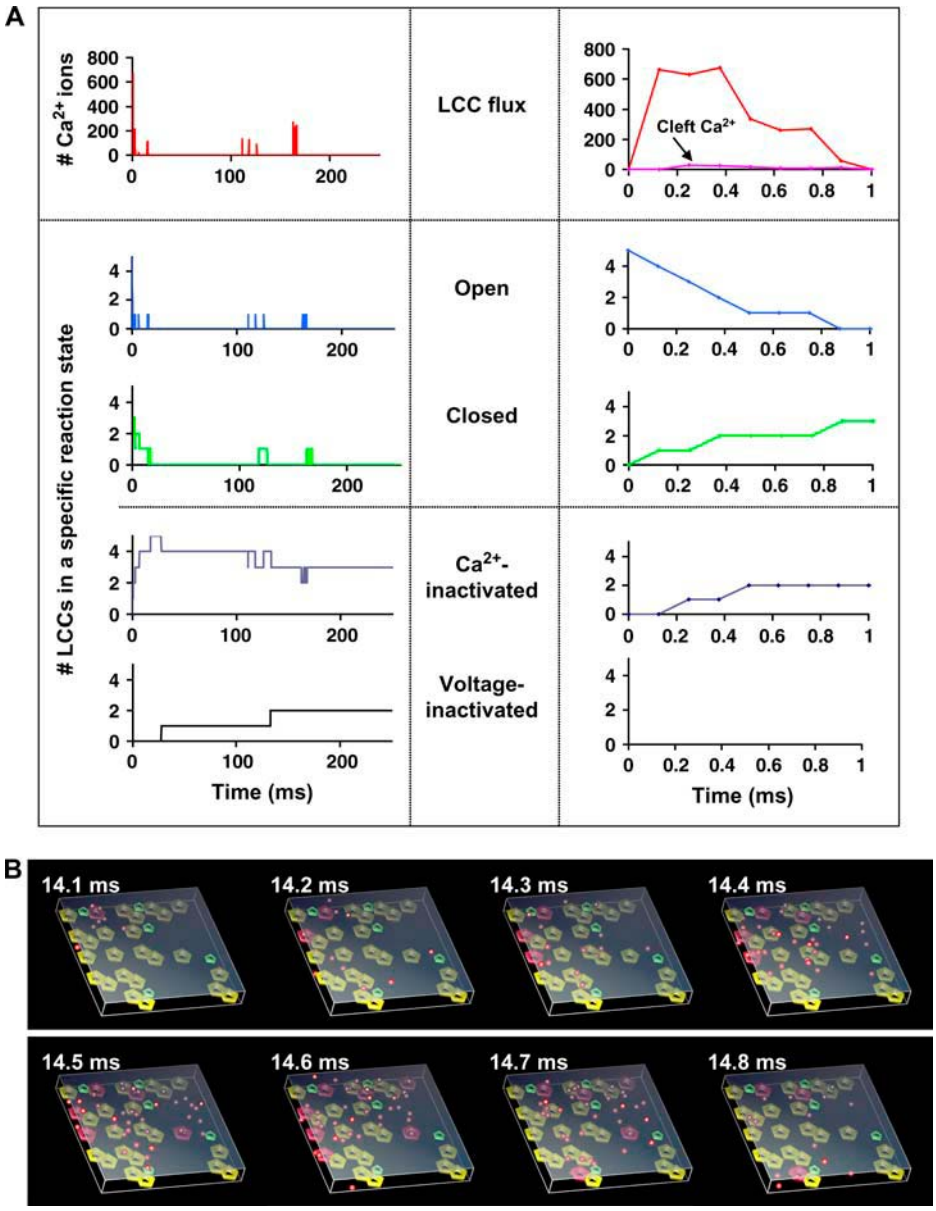

FIGURE 3 (*A*) Single-trial data on LCC flux, gating, and inactivation for the entire simulation duration (250 ms, *left panels*) and in higher time resolution (first ms, *right panels*). Data are obtained from a cleft model of $D_{cleft} = 12$ nm and $L_{cleft} = 100$ nm, containing five LCCs and 25 RyRs. No RyR activation or LCC voltage inactivation is observed in the first ms. The top traces track LCC flux, whereas the remaining traces track LCC activity in specific reaction states per time point. The top right trace also depicts the precise number of Ca^{2+} ions present in the cleft for the first ms, and when compared to the total LCC flux (of >10 times greater magnitude), can demonstrate that diffusion-mediated Ca^{2+} efflux occurs rapidly. (*B*) Representative visualization of activity (0.1 ms per frame) in the model described in Fig. 3 *A*. The TT membrane (*top*, *shaded*) bears five LCCs (*green*) that have all been Ca^{2+}- or voltage-inactivated at 14 ms into the simulation. The SR membrane (*bottom*, *unshaded*) bears 25 RyRs in the closed (*yellow*) or open (*red*) states. Free Ca^{2+} ions are depicted as red spheres. This frame sequence illustrates a propagating pattern of RyR activation that is evident by following the open RyRs as time progresses.

The MCell simulation environment

MCell uses Monte Carlo algorithms (by pseudorandom number generation) to stochastically describe 3D Brownian random-walk diffusion and chemical reaction kinetics in complex spatial environments (www.mcell.cnl.salk.edu, (56)). Reaction transition probabilities are calculated according to user-specified rate constants, and compared to the value of a generated random number to decide the succeeding reaction state. The user defines the model using a special model description language, which MCell will parse to create corresponding C++ objects and simulations according to user instructions. To model a system using MCell, it is necessary to specify 1) geometry of the subcellular ultrastucture; 2) diffusion constants of diffusing ligands; 3) positions of effector sites that interact with ligands; 4) chemical reaction mechanisms and kinetic rate constants governing the system; and 5) an appropriate time step and the number of Monte Carlo time steps or iterations to simulate.

Simulations were performed on a dual Xeon 1.0 GHz workstation running the Hummingbird Exceed 8.0 X-server. It took ~3 min of computer time to simulate 100 ms of real time. To speed up simulations, we used the MCell runtime optimization method of 3D spatial partitioning. Spatial partitions are transparent planes that the user places to create subvolumes in the modeled space, thus reducing the computation power required to track the movements of individual molecules to each subvolume. In this manner, computing speed is less dependent on microdomain complexity. MCell allows the user to export simulation results into visualization data formats for a variety of graphic tools. In this study, 3D images were rendered with IBM Data Explorer (www.opendx.org) using the companion visualization package DReAMM (www.mcell.psc.edu/DReAMM).

RESULTS

Having established a Monte Carlo model of a dyadic cleft, one can try to investigate the properties of Ca^{2+} release within the cleft following a depolarization protocol representative of the voltage changes in an AP. Deterministic and

partially deterministic models of myocyte Ca^{2+} release (4,7,57) have tracked LCC mediated responses to changes in membrane potential during the course of an AP using, e.g., Hodgkin-Huxley-type equations. Experimentally and theoretically, it has been determined that at the initiation of an AP, the cardiac ventricular sarcolemmal membrane experiences a sharp depolarization from around −80 mV to +20 mV followed by a gradual repolarization. Moreover, for more than three-quarters of an AP, the cardiac ventricular sarcolemmal membrane resides in the near-zero to positive potential range, implying that membrane potential does not change drastically much of this time, and that approximating the voltage dependence of LCC parameters will not critically affect dyadic cleft [Ca^{2+}]. This assumption is further supported by findings that Ca^{2+}-mediated inactivation is a more significant mode of LCC inactivation than voltage inactivation (58). In addition, although LCC currents play a major role in activating Ca^{2+} release from the jSR, they do not contribute significantly to the subspace [Ca^{2+}] once SR release has been triggered. Thus Ca^{2+} spark duration and magnitude is relatively independent of the triggering sparklet (37). These considerations have prompted us to suggest that a simplified LCC simulation reflecting a voltage-clamp scenario can be a sufficiently accurate representation of trigger Ca^{2+} influx. An added benefit of this assumption is the possibility of defining the voltage-dependent parameters used in the model (unitary current, the rate of voltage-inactivation, and channel gating kinetics) to be equivalent to those experimentally determined under actual voltage-clamp conditions (0 mV, +10 mV, and +20 mV (37,44,43)). We thus assume throughout this study that the TT membrane is voltage-clamped at the beginning of each simulation to ~+10 mV and remains so for the entire response duration.

To confirm that LCC inactivation is primarily Ca^{2+}-mediated, we tracked the LCC behavior in a dyadic cleft of $L_{cleft} = 100$ nm and $D_{cleft} = 12$ nm, containing five LCCs and 25 RyRs. At any time point, each of the five LCCs may exist in the open (conducting), closed, Ca^{2+}-inactivated, or voltage-inactivated states. Fig. 3 *A* shows representative single-trial data on LCC flux, gating, and inactivation for the entire simulation duration (*left panels*), and, in greater detail, events that take place in the first millisecond (*right panels*). Note that in the initial phase of membrane excitation none of the RyRs have yet been activated by the trigger Ca^{2+}. Since Ca^{2+} and voltage inactivation are known to be independent processes (46), here we assume that Ca^{2+}-inactivated LCCs can also be voltage-inactivated. These traces show that Ca^{2+} inactivation of some of the LCCs can occur as early as <1 ms after the onset of the AP, whereas maximum Ca^{2+} inactivation (involving all five LCCs in the cleft) is reached within the first 20 ms. Voltage inactivation, on the other hand, gradually sets in later at ~40 ms after the onset of the AP. Overall, the LCC opening events are distributed stochastically, with some instances of ''bursts'' representing a few openings in rapid succession. Note that although up to 650 Ca^{2+} ions are generated into the cleft in the first millisecond, the corresponding maximum Ca^{2+} level in the cleft amounts to only ~50 ions. It is apparent that a vast majority of Ca^{2+} ions released into the modeled cleft are expected to diffuse rapidly into the surrounding cytosolic space. Fig. 3 *B* is a visual representation of sequential events in the cleft during the 14th ms, at a resolution of 0.1 ms per frame. At this time, all five LCCs (*smaller hexagons*, *top surface*) have been either Ca^{2+}- or voltage-inactivated. The influx of Ca^{2+} ions (depicted as *red spheres*) in the cleft is observed to correspond to the spatial propagation of RyR (larger hexagons, bottom surface) activity. A more detailed view of Ca^{2+} influx over the first 5 ms is given in the Supplementary Material.

To determine the Ca^{2+} response within a single cleft after the onset of depolarization, we determined the number of Ca^{2+} ions within a standard cleft ($L_{cleft} = 100$ nm, $D_{cleft} = 12$ nm) as a function of time (Fig. 4 *A*). The single-cleft Ca^{2+} response (*inset*) shows that the number of Ca^{2+} ions can vary from zero to 60 ions over the course of a simulation, whereas the peak of the Ca^{2+} response averaged from 100 independent trials is only ~23 ions. Thus, the average, predicted response is clearly far from deterministic and is subject to substantial stochastic variations. For the case of the standard cleft, the predicted Ca^{2+} response reaches a peak after 9.75 ms, gradually declining to basal levels by the end of 200 ms. This model reproduces critical features of experimentally observed Ca^{2+} sparks. In particular, the time to peak for the Ca^{2+} response is very similar to that previously recorded for Ca^{2+} sparks in mouse ventricular myocytes (10 ms) using confocal image analysis (59). At each given time, low numbers of ions in the cleft will translate into significant magnitudes of [Ca^{2+}] due to the small cleft volume (1.2×10^{-13} μL). The peak of the average response, for instance, is ~300 μM. This value is significantly higher than the estimates presented in some previous deterministic and semistochastic models (4), but is consistent with other estimates (3). It is instructive to consider that a single Ca^{2+} ion within the assumed dyadic cleft volume would be equivalent to ~13 μM, which is also above the range given in many modeling and experimental estimates. The significance of predicting these relatively high levels of Ca^{2+} in dyadic spaces will be discussed below.

One of the main goals of this study was to investigate the dependence of Ca^{2+} response on the geometry of the dyadic cleft. It has been reported that the dimensions of the dyadic spaces may vary in different species, and also during myocyte development in the same species. In addition, it has been suggested that myocyte remodeling during heart failure may contribute to a changed dyad geometry, possibly through increased separation between the TT and SR membranes (40). To address the importance of the proximity of these two membranes confining a dyadic cleft, we have progressively changed the membrane separation (D_{cleft}) from 9 to 40 nm. This variation resulted in significant changes in the peak of

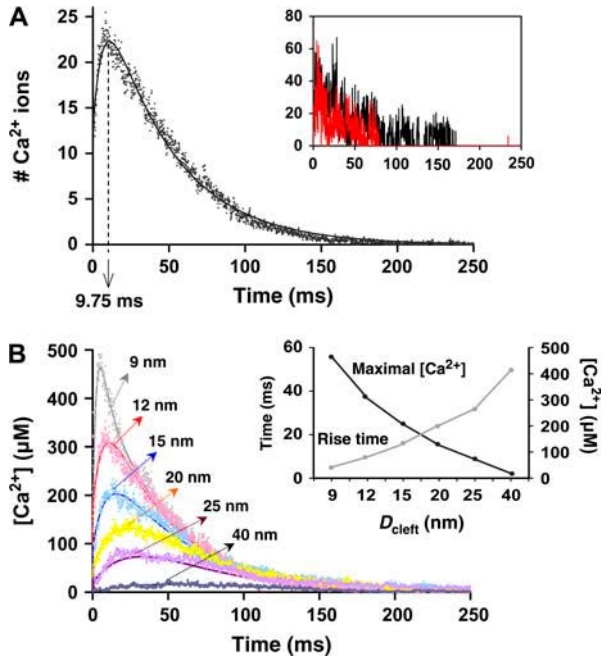

FIGURE 4 The Ca^{2+} response after the onset of depolarization as a function of time. Each simulated cleft consists of five LCCs and 25 RyRs, and a standard L_{cleft} of 100 nm. (*A*) We first observe the response in a cleft with the assumed normal membrane separation of $D_{cleft} = 12$ nm, averaged from 100 independent trials. The averaged number of Ca^{2+} ions in the cleft (*scatter plot*) is fit to an exponential function (*smooth curve*) consisting of one rise-time constant and 1 decay-time constant. The predicted rise time of 9.75 ms is very close to that previously measured in Ca^{2+} sparks using rat ventricular myocytes. The inset shows results from two separate, single trials depicting the stochasticity of Ca^{2+} release. (*B*) D_{cleft} is progressively varied from 9–40 nm to study the effects of geometry changes in the cleft. After the onset of each AP, the Ca^{2+} level reaches a peak after ~5–50 ms and gradually declines after 150 ms. The model demonstrates how, e.g., doubling of D_{cleft} from 12 nm to 24 nm, will result in a markedly reduced $[Ca^{2+}]$. Further increasing the intermembrane distance to 40 nm produces a fluctuating trace of extremely low $[Ca^{2+}]$, a condition which might lead to altered contractile properties of the myocyte. The inset shows the dependence of rise time and peak $[Ca^{2+}]$ on D_{cleft} (*x* axis not to scale). This model corresponds qualitatively to results from earlier deterministic models of Ca^{2+} release.

the amplitude of the response, whereas the response duration was not significantly affected (Fig. 4 *B*). More precisely, the $[Ca^{2+}]$ responses over time were averaged over 100 runs and fitted with a sum of two exponentials, describing the rise to the peak and the subsequent decline in $[Ca^{2+}]$. The rate of the rise in $[Ca^{2+}]$ displays significant variation with D_{cleft}. Accordingly, we also find that the frequently measured ''rise time,'' defined as the time between the onset and peak of the response, displays high sensitivity to the cleft geometry. This is evident where the rise time consistently increases while D_{cleft} is progressively increased (Fig. 4 *B*, *inset*). The estimated rise time increases from 5 to 50 ms, with the 9.75-ms rise time for $D_{cleft} = 12$ nm displaying the closest correlation to previously reported values (see, e.g., Wang et al. (29,37) and Bers (59)). The peak $[Ca^{2+}]$, on the other hand, decreases systematically with an increase in D_{cleft}, indicating a possible loss of LCC/RyR coupling due to spatial separation (Fig. 4 *B*, *inset*) leading to compromised Ca^{2+} signaling efficiency.

Since the size of the dyadic cleft can also vary in terms of the dimensions of the TT and SR membranes (in addition to the gap separating them), we have also analyzed the dependence of Ca^{2+} response on the larger, *x,y* dimensions of the cleft (L_{cleft}). In particular, square membrane portions of 100–500-nm dimensions were analyzed for a constant D_{cleft} of 12 nm. Interestingly, the amplitude of Ca^{2+} response showed very little sensitivity to L_{cleft} in the 300–500 nm range, whereas the response was increasingly more pronounced as L_{cleft} was varied from 200 to 100 nm (Fig. 5 *A*). Overall, the amplitude of the response for the assumed D_{cleft} of 12 nm varied less than twofold. The rise-time variation was modest, changing marginally between 8.25 and 9.75 ms (Fig. 5 *B*). These results suggest that the dimensions of the TT and SR membranes might not be crucially important in determining the properties of a spark. Indeed, if one considers that changing L_{cleft} from 300 to 500 nm would result in an approximately threefold increase in the cleft volume and a ~1.5-fold increase in the area of the ''side walls'' through which Ca^{2+} is assumed to escape, one sees that these geometry changes are comparatively similar to the increases in volume and escape area resulting from the

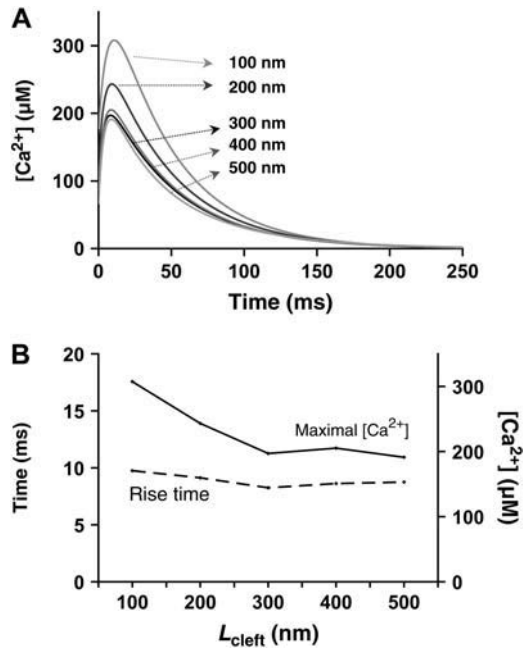

FIGURE 5 (*A*) $[Ca^{2+}]$ as a function of time in clefts containing five LCCs and 25 RyRs. D_{cleft} is fixed at 12 nm, whereas L_{cleft} ranges from 100–500 nm. (*B*) The dependence of peak $[Ca^{2+}]$ and rise time on L_{cleft}. The amplitudes of these parameters change modestly with L_{cleft}, in contrast to a higher dependence on D_{cleft} (Fig. 4 *B*, *inset*). These results suggest that membrane separation is likely to play a greater role in Ca^{2+} regulation than the lateral-cleft dimensions.

increases in D_{cleft} from 9 to 25 nm and from 9 to 15 nm, respectively. However, the described change to L_{cleft} results in virtually no decrease in the peak [Ca^{2+}], whereas the corresponding changes to D_{cleft} result in approximately six- and twofold decreases in the peak [Ca^{2+}].

Confocal imaging has been successfully used in conjunction with patch-clamping to visualize Ca^{2+} influx corresponding to single sparks and sparklets (29,37). In these studies, Wang et al. introduced a way to characterize the ''signal mass'' of sparklets by measuring the space-time integral of the associated Ca^{2+} dye fluorescence intensity. A linear correlation between the visualized ''signal mass'' and the actual time-integrated Ca^{2+} influx has been observed. To investigate the quantitative and qualitative relation between the channel flux and Ca^{2+} present in the model, we adopt the above-described correlation method. We determine the dependence of the time integral of the number of Ca^{2+} ions in the cleft on the time integral of Ca^{2+} influx through both types of channels (also equal to sum total of Ca^{2+} efflux), taken over the time course of simulation of single sparks (Fig. 6 *A*). The stochasticity of the response was evident in the ranges of the integrals for individual sparks spanning an order of magnitude, in qualitative agreement with the variation of Ca^{2+} influx observed by Wang et al. (37). For each specified geometry, the integrals displayed excellent linear correlation. The slopes of the lines indicate the capacity of the clefts to transiently accumulate Ca^{2+} ions. In particular, the slopes obtained in Fig. 6 *A* (0.76, 0.29, and 0.04) are directly related to the corresponding cleft volumes (3.0×10^{-12} μL,1.08×10^{-12} μL, and 1.2×10^{-13} μL), suggesting that the cleft volume is the main determinant of total Ca^{2+} accumulation for the constant D_{cleft} of 12 nm. However, should D_{cleft} be varied (Fig. 6 *B*), the slopes of similar correlations do not significantly differ from each other, even though the cleft volume may differ approximately fourfold. This indicates that an increased coupling between LCC and RyR may compensate the decreased capacity for Ca^{2+} accumulation in smaller cleft volumes. Within the same cleft dimensions, we found that no correlation was present between the total Ca^{2+} influxes through LCCs and RyRs (Fig. 6 *C*). This result provides additional evidence that RyR behavior is predominantly independent of LCC currents, and that LCC currents serve only as a trigger to regulate the onset, but not the entire time course, of the spark. In sum, [Ca^{2+}] during a spark development is mediated primarily by RyR and not LCC. The data presented in Fig. 6, *A–C*, suggest that, at least for the purposes of determining [Ca^{2+}] in a cleft, the assumed size (*x,y* dimensions) of a dyadic cleft is not as significant as the intermembrane separation. This finding further supports the importance of proximity of LCC and RyR molecules in Ca^{2+} spark regulation.

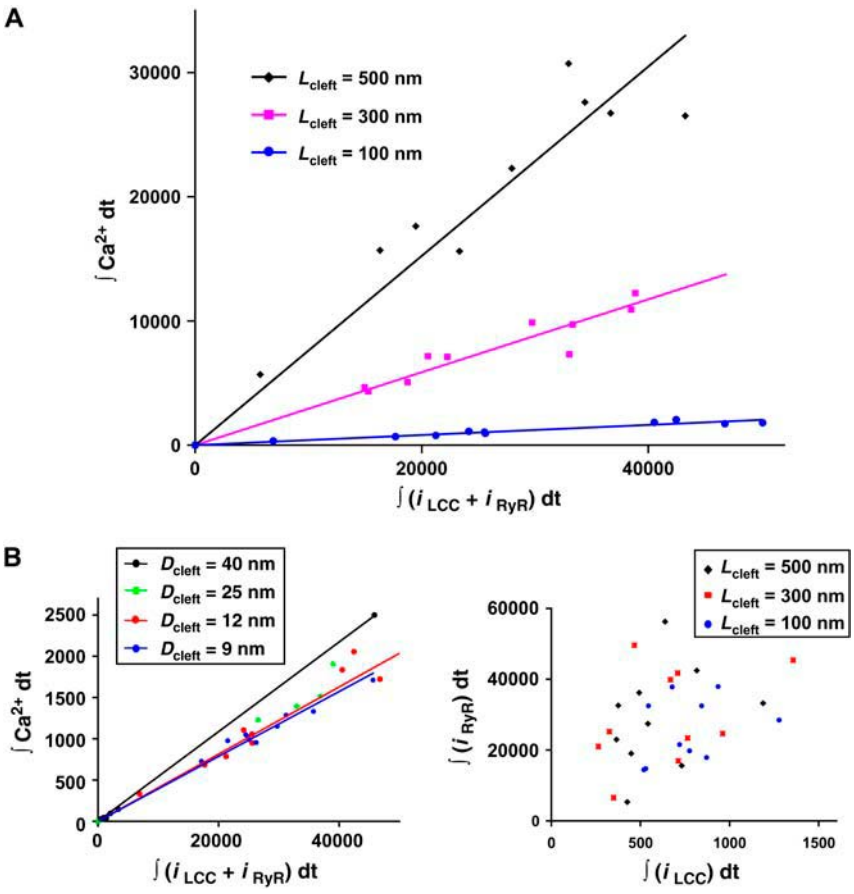

FIGURE 6 To investigate the relationship between the channel influx and the amount of Ca^{2+} present in the cleft, we obtain the integrals of these two parameters over time. (*A*) Correlations between the time integral of Ca^{2+} influx ($\int (i_{LCC} + i_{RyR})dt$), and the sum total of Ca^{2+} residing in the cleft ($\int Ca^{2+}dt$), taken over the entire duration of each simulation. L_{cleft} ranges from 100 to 500 nm, whereas D_{cleft} is unchanged at 12 nm. (*B*) D_{cleft} ranges from 9 to 40 nm, whereas L_{cleft} is unchanged at 100 nm. Each line represents the correlation between channel influx and cleft Ca^{2+} for a particular geometry. When only L_{cleft} is changed, as in panel *A*, the magnitudes of the slopes exhibit a dependence on the cleft volumes. This is not observed when only D_{cleft} is varied, as in panel *B*. It is possible that greater membrane separation increases the cleft volume and its capacity to transiently store Ca^{2+}, while compromising LCC/RyR coupling efficacy. The tradeoff between cleft volume and channel coupling can account for the resulting similar slopes for clefts of different volumes upon variation of D_{cleft}. (*C*) The time integral of Ca^{2+} influx through LCCs is compared with that through RyRs. No correlation is evident, suggesting that LCC currents serve only as a trigger regulating the onset of spark development, and that SR release is independent of LCC influx much of the time.

So far we have considered a single dyadic cleft. However, it is important to see whether coupling between several clefts will affect Ca^{2+} regulation. Neighboring clefts are thought to be spaced ~2 μm apart longitudinally (across neighboring sarcomeres) and 0.2–0.8 μm transversely (down the transverse tubule/in the plane of the Z-line) (9,60–62). During the course of a Ca^{2+} spark, local [Ca^{2+}] may reach high values. However it is usually assumed that Ca^{2+} dissipates rapidly between the clefts to levels that are too low to activate release events in neighboring clefts. To investigate how local [Ca^{2+}] will be affected when the spatial separation between clefts is removed, we modeled a test case where multiple clefts are compacted adjacent to one another (illustrated in Fig. 1 *C*). Here, we define that a cluster of channels consisting of five LCCs and 25 RyRs is equivalent to one ''CaRU.'' The resultant conjoint dyadic cleft will have dimensions $L_{cleft,1} =$ 100 nm and $L_{cleft,2} = 400$ nm, and consist of 20 LCCs and 100 RyR molecules (four CaRUs). Compared to a single cleft where $L_{cleft} = 100$ nm (containing one CaRU), this new space gave rise to a 2.75-fold increase in peak amplitude to 0.85 mM, and much shorter rise time of ~3 ms. This maximal [Ca^{2+}] approaches a level close to the extracellular and lumenal [Ca^{2+}] of 1 mM. The effect of the ''stacked'' morphology on simulated spark properties can be further analyzed by comparisons to square dyadic clefts of the same volume ($200 \times 200 \times 12$ nm^3) containing either the standard assumed single CaRU or, to preserve relative stoichoimetry, the denser configuration of four CaRUs. In fact, the quantity of channels in four CaRUs is similar to that commonly assumed in modeling analyses (5). The response curves suggest that the stacked geometry results in an approximately threefold increase in [Ca^{2+}] amplitude compared to that containing a single CaRU, and an approximately twofold lower response compared to the square cleft containing four CaRUs. The response peak of 1.6 mM in the case of four CaRUs ($L_{clef} = 200$ nm) is likely to be too close to (or higher than) the lumenal [Ca^{2+}] to be physiologically relevant, suggesting that lumenal Ca^{2+} can be transiently depleted in this case, pushing the current model to the limit of applicability. Nevertheless, we attempted to analyze the dependence of Ca^{2+} responses in the stacked geometry ($L_{cleft,1} = 100$ nm, $L_{cleft,2} = 400$ nm) and the square cleft ($L_{cleft} = 200$ nm), both containing four CaRUs, on a variation in D_{cleft} (Fig. 7 *B*). Not unexpectedly, the peaks of the responses were very sensitive to D_{cleft}, varying approximately four- to sixfold. The rise time was significantly lower than that assumed in the standard geometry, being <5 ms for most of the geometries assumed. Overall, the results in Fig. 7, *A* and *B*, suggest that increasing the numbers of LCCs and RyRs per dyad can result in significant increases in [Ca^{2+}]—a scenario that may not be physiologically plausible.

Binding of β-adrenergic agonists such as norepinephrine and isoproterenol to the β-AR or sarcolemma of ventricular myocytes increases intracellular levels of cAMP via G_s-protein induced stimulation of adenylyl cyclase. cAMP in turn activates PKA, which causes phosphorylation of proteins involved in Ca^{2+} homeostasis, such as phospholamban, LCC, and RyR. This cascade of events leads to an increase in the [Ca^{2+}] transient, and to a positive inotropic effect. In normal, healthy cardiomyocytes, acute β-adrenergic stimulation might be a part of the ''fight or flight'' response, resulting in enhanced EC coupling, higher [Ca^{2+}]$_i$ transients, and faster pacing. In myocytes from failing hearts, however, there has been evidence of chronically high β-adrenergic stimulation and, paradoxically, decreased rates of contraction and relaxation and depressed Ca^{2+} transients. Moreover, it has been suggested that the coupling between LCC and RyR can be diminished in states preceding chronic heart failure, e.g., in postmyocardial infarction myocytes, due to geometric reorganization of dyadic clefts. To explore the

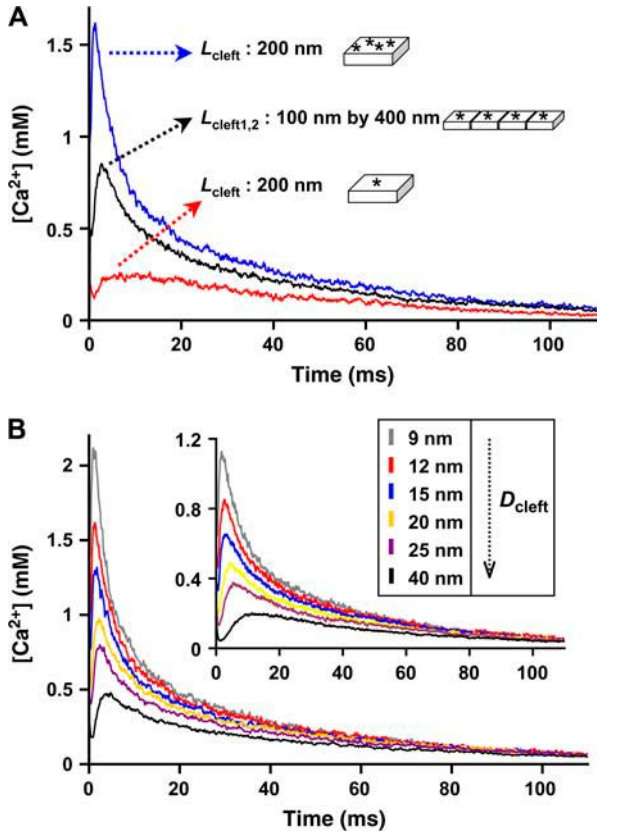

FIGURE 7 (*A*) Effects of varying geometry and channel density in models of $D_{cleft} = 12$ nm. Each CaRU is defined to be a cluster of five LCCs and 25 RyRs, and is denoted by a single asterisk in the figure. We first compare two models of similar dimensions ($L_{cleft} = 200$ nm; square *x*,*y* dimensions), with one containing four CaRUs (*blue*) and the other containing one CaRU (*red*). To investigate how local [Ca^{2+}] will be affected when the spatial separation between clefts is removed, we also model a test case where $L_{cleft,1} = 100$ nm and $L_{cleft,2} = 400$ nm. This is equivalent to compacting multiple clefts adjacent to one another (see visualization in Fig. 1 *C*). (*B*) Comparison of models containing four CaRUs, across values of D_{cleft} ranging from 9 to 40 nm. The main figure depicts [Ca^{2+}] as a function of time for the model of $L_{cleft} = 200$ nm, whereas the inset depicts the same for the model of $L_{cleft,1} =$ 100 nm and $L_{cleft,2} = 400$ nm. Due to the rapid decay of Ca^{2+} response, the timescale for this figure is presented up to only 100 ms.

potential role of PKA-mediated phosphorylation in dyadic clefts of various geometries, we extended our model to include the experimentally determined characteristics of LCC and RyR functions in phosphorylated states (Fig. 8). In the simulations we assumed that various percentages of LCCs and RyRs can be phosphorylated, so that their gating properties become altered (see Methods for details). Phosphorylation of Ca^{2+} channels was found to progressively increase the amplitude of the peak up to sixfold when the phosphorylation status was varied from 0 to 100%. The [Ca^{2+}] profiles converged rapidly at ~20 ms due to rapid decay, after which they diverged steadily, with profiles for higher degrees of phosphorylation attaining basal Ca^{2+} levels earlier. Based on these profiles, it is likely that high levels of channel phosphorylation can lead to both accelerated and enhanced Ca^{2+} transients, which in turn can alter contractile properties. The quick onset of the Ca^{2+} response in the event of phosphorylation was primarily a consequence of the almost immediate opening of RyRs after the AP initiation. In sum, the phoshorylation data suggest that the spark properties can be significantly affected by adrenergic signaling serving as an easily adjustable regulator of EC coupling.

In separate studies on the effects of Ca^{2+} buffering, we have incorporated in our model immobile Ca^{2+}-binding molecules that bear parameters of known endogenous Ca^{2+} buffers. An L_{cleft} of 200 nm was selected to allow us to test the effects of saturating the cleft with a large amount of buffer molecules (110 on the SR membrane and 125 on the TT membrane) as opposed to a moderate level of buffers (50 on each membrane). In every case, the standard stoichiometry of five LCCs and 25 RyRs per cleft was used. For each level of buffering intensity, we compared the extreme cases of strong binding affinity (modeled after troponin C) and low binding affinity (modeled after inherent sarcolemmal-membrane Ca^{2+} buffering) using known buffering reaction kinetics (55). The results, as shown in Supplementary Material, indicate that the effects of buffering are sensitive to neither the amount of buffers nor the buffering intensity. The averaged Ca^{2+} responses for all buffered cases decreased in peak by approximately five ions compared to the nonbuffered case, but otherwise remained unchanged in terms of rise time and rate of decay. It is possible that rapidly diffusing Ca^{2+} escapes so readily from the small cleft volume that any effects of momentary Ca^{2+} removal due to buffering become negligible. The strong positive feedback mechanism of CICR could also contribute to the insensitivity of the Ca^{2+} response to buffering.

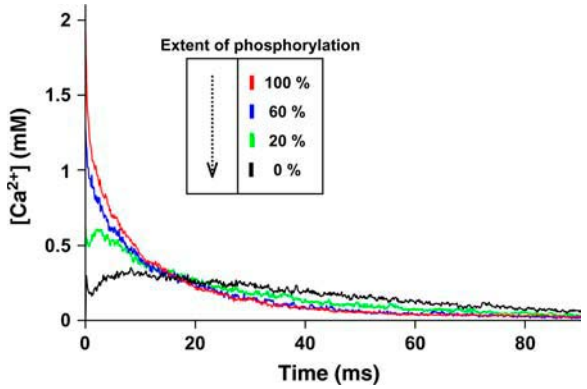

FIGURE 8 Effects of different levels of LCC and RyR phosphorylation in clefts containing five LCCs and 25 RyRs. The extent of channel phosphorylation was varied from 0% to 100% to investigate its influence on Ca^{2+} release (see Methods for detailed description). Phosphorylation of Ca^{2+} channels was found to progressively increase the amplitude of the peak response up to sixfold. One possible consequence is an alteration of myocyte contractile properties. Due to the rapid decay of Ca^{2+} response, the timescale for this figure is presented up to only 80 ms.

Establishing a fully stochastic model of Ca^{2+} regulation events in a dyadic cleft provides one with the advantage of being able to study the level of ''noisiness'' of the response. In particular, an important question relevant to the notion of local control of EC coupling is whether the localized Ca^{2+}-release events are predicted to be too stochastic to exert any reasonable control of Ca^{2+} efflux from a dyadic space or of local contraction regulation. Another way this question can be put is ''how distinct is the Ca^{2+} concentration in a single dyad from the average Ca^{2+} concentration produced by multiple sparks in multiple dyads that characterizes the whole cell level of contraction control?'' If the deviation from the average Ca^{2+} level is strong, one can ask how many dyadic clefts should contribute to the local output to render the local response sufficiently close to the average to ensure robust contractility regulation. We have addressed this question by determining the number of Ca^{2+} ions in a standard dyadic cleft over 250 ms. It is evident (Fig. 4 *A*, *inset*) that single dyadic cleft responses can be significantly different in terms of both amplitude and duration of response from the average of multiple simulated dyadic-space responses (Fig. 4 *A*). It follows that to achieve the level of control suggested by the average [Ca^{2+}] response, the outputs from several dyadic spaces may need to be coupled to attain the final contraction output. To assess the noise reduction with the number of summed up dyadic spaces we measured the deviation of the responses averaged over a varying number of clefts from the average of response for 100 clefts according to the following formula:

$$X_n = \frac{1}{N_\tau}\sum_\tau \frac{|[Ca^{2+}]_\tau - [Ca^{2+}]_{avg,\tau}|}{[Ca^{2+}]_{avg,\tau}}, \quad (1)$$

where τ is a time step in a simulation. We found that for the normal assumed cleft geometry X_n is reduced on average by 30%, if responses of 10 clefts are averaged, and by ~50% for 20 clefts, compared to the average X_n value for a single cleft (Fig. 9). Thus the combined output can closely approach the true average spark response if 10–20 dyadic clefts contribute to it in a coordinated fashion. AP propagation can serve to synchronize the onset of the sparks so that the ''averaging'' is efficiently performed by the cell.

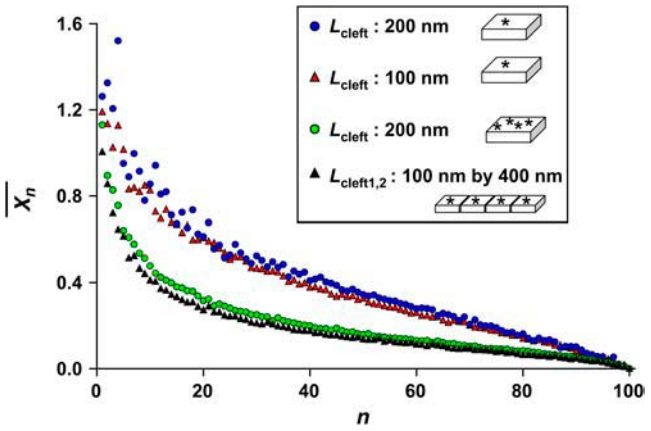

FIGURE 9 The stochasticity of Ca^{2+} signaling can be moderated if Ca^{2+} efflux from a relatively small number of clefts can be averaged in the downstream Ca^{2+}-dependent events. The noise metric introduced in Eq. 1 is plotted as a function of the number of integrated dyadic clefts of different dimensions. Our estimates indicate that if the Ca^{2+} responses from 10–20 dyadic clefts are integrated, the noise in the Ca^{2+} output can be reduced by up to 50%.

DISCUSSION

Here we describe a 3D Monte Carlo model of the dyadic cleft, a fundamental site of Ca^{2+} release. In the development of the model, we seek to provide a mechanistic view of the events underlying Ca^{2+} spark formation and, in turn, understand how the spatially restricted microenvironment of the dyad could affect spark properties. Under physiological conditions, Ca^{2+}-mediated coupling between LCCs and RyRs exhibits stochastic kinetics, a phenomenon caused in part by the small cleft volume ($\sim$1.0–20.0 $\times$ 10^{-19} L), as well as the stochastic nature of channel gating and diffusion processes within these local domains (3–7). If one were to model this system in a fully deterministic way, it would be necessary to assume that the concentrations of participating molecular species do not undergo discontinuous changes due to the finite numbers of the corresponding molecules. Within dyadic clefts, however, this assumption fails, as Ca^{2+} fluxes from the SR and extracellular space resulting in appearance of relatively few ions can create very high local Ca^{2+} concentrations (6). Given the above reasons, we have employed a completely stochastic approach to help us understand Ca^{2+} regulation events in the dyadic cleft.

This model allowed us to incorporate a variety of experimentally determined parameters of Ca^{2+} regulation into simulations, where channels and ions were traced as stochastically behaving molecules embedded in a simplified geometry bearing dimensions reported for real dyadic clefts. Ca^{2+} ions, often as few as less than a dozen per cleft at the peak of Ca^{2+} generation, were modeled as particles undergoing random walks. Thus, the model provided us with a realistic view of spatially inhomogeneous stochastic processes involved in a localized Ca^{2+} response. LCC and RyR molecules were also described in a stochastic manner by incorporation of complex regulation schemes based on previously reported single-channel data.

Previous mathematical descriptions of LCC behavior were based on mode-switching between normal and Ca^{2+}-inactivated states, governed by a rate constant that is a function of subspace Ca^{2+} concentration (4,63). This method of modeling can account for the Ca^{2+}-dependent behavior of the LCC, assuming that Ca^{2+} levels are well averaged throughout the modeled space. However, as described above, localized fluctuations of Ca^{2+} levels in the cleft might be significant enough to render such a deterministic method inaccurate and unreliable. One of our goals was to describe the stochastic effects in this system at the level of individual ions. For instance, when we modeled the Ca^{2+}-inactivation mechanism, we accounted for the binding kinetics of individual Ca^{2+} ions to CaM (46), as opposed to deterministic methods where [Ca^{2+}] is approximated. We based our description of LCC Ca^{2+}-dependent inactivation on a study by Peterson et al. (48), which suggested that the high-affinity sites of CaM, not the low-affinity sites, are responsible for this process. The LCC reaction scheme in this model reflects the above experimental findings by accommodating two Ca^{2+}-binding events before the Ca^{2+}-inactivated state is attained (Fig. 2 *A*).

Unitary RyR Ca^{2+} currents have been measured in artificial bilayers under conditions that often underestimate the level of multiple ions present in physiological solutions (64,65). This has led to the belief that unitary current is close to a large value of $\sim$0.35 pA, as opposed to other observations that estimate unitary RyR current to be $\sim$0.1 pA. The discrepancy can be explained by experiments (50) that demonstrate that physiological levels of monovalent cations and Mg^{2+} are able to compete effectively with Ca^{2+} as a charge carrier in cardiac RyR. Experiments performed in artificial conditions, where lumenal [Ca^{2+}] is extremely high (up to 20 mM) and competing charge carriers are absent, may have produced amplified unitary RyR current values. We adopt a unitary RyR current of $\sim$0.1 pA in our simulations.

One aspect of RyR behavior we did not account for is the possibility of array-based interactions like coupled gating and inhibitory feedback (51). As pointed out in Methods, the exact number of RyRs necessary to produce a spark remains controversial, which is compounded by limited knowledge about the nature of RyR recruitment and array-based RyR interactions. It has been observed that RyRs incorporated into artificial lipid bilayers can exhibit coupled gating (66), a process that may be mediated by FK-binding proteins (FKBP) associated with neighboring RyRs (67,68). Sobie et al. (5) had previously described a model where neighboring RyRs are complexed into homotetramers through FKBP association, and all RyRs in each homotetramer gate in unison. This manner of RyR description brings to mind the quantal nature of Ca^{2+} sparks reported recently by Wang et al. (29),

who proposed that the quantal nature of Ca^{2+} sparks is revealed based on spark-flux histograms that exhibit distinct, regular peaks that are multiples of 1.2 pA. In our model, however, the RyR is described as an independent, individual unit that is not physically associated with any other protein. We made this approximation in the initial stochastic simulation, bearing in mind that the exact mechanisms of many RyR array-based interactions are not yet available in the literature.

An important result of the simulations presented in this study is that the incorporation of single-channel parameters (mostly determined in patch-clamp experiments) was sufficient to reproduce many aspects of in vivo Ca^{2+} spark generation with minimal extra assumptions. For example, it was assumed that no buffer molecules were present within the cleft; further studies presented in Supplementary Material suggest that buffering indeed exerts negligible effect on local Ca^{2+} levels. We also observed that regardless of the assumed Ca^{2+}-dependent inactivation rate of the RyR, dynamical characteristics of averaged Ca^{2+} sparks, such as rise time and duration of the initial phase of response, were predicted by the model with a degree of accuracy.

Significantly, it was also determined that individual sparks are likely to be highly variable and display highly stochastic dynamics. The variability, evident from the comparison of Ca^{2+} time courses corresponding to individual sparks, results in a range of up to 10-fold in terms of total Ca^{2+} outflux and $[Ca^{2+}]$ during spark generation. This variability suggests that although individual sparks are likely to be completely uncoupled, any degree of local control requires the integration of input from at least several sparks for downstream contraction regulation. Our estimates indicate that if 10–20 synchronized sparks are combined, the noise in the output can be reduced by up to 50%. In such a case one can argue that deterministic rather than stochastic models can be used to describe EC coupling without much error. These results suggest that the local control theory might need to be modified to assume a synchronized effect of several dyads in a local setting, in order for it to predict the macroscopic consequences of CICR.

Several previous studies have determined that the geometry of dyadic clefts can range widely across species as well as within the same species during development and disease. In addition, many crucial proteins involved in EC coupling are concentrated at the TT, suggesting that TT structure can play an important role in regulating cell function (69). We have thus studied the role of geometry alterations in the regulation of Ca^{2+} sparks during an AP. We found that the sensitivity of $[Ca^{2+}]$ response was much greater to changes in the size of the gap separating the sarcolemma and the SR membranes than to changes in the assumed size of a dyadic cleft (the lateral dimensions of the membrane bounding the cleft). High sensitivity of the Ca^{2+} response to intermembrane separation was evident in terms of both the variation of the rise time and amplitude of $[Ca^{2+}]$.

The results of the study provide numerical evidence that Ca^{2+} sparks arising during AP propagation are particularly robust to variation in the cleft size, in terms of both the rise time and $[Ca^{2+}]$ peak values, when the intermembrane gap is close to its physiological value of 12 nm. The divergence of estimates of lateral cleft size (x,y dimensions) presented in the literature is thus likely to be of minor consequence for quantitative aspects of $[Ca^{2+}]$ response, given a constant number of channels per cleft.

SUPPLEMENTARY MATERIAL

An online supplement to this article can be found by visiting BJ Online at http://www.biophysj.org.

We are grateful to Raimond L. Winslow, Joseph L. Greenstein, and Henry M. Colecraft for useful discussions.

REFERENCES

1. Niggli, E., and P. Lipp. 1993. Subcellular restricted spaces: significance for cell signalling and excitation-contraction coupling. *J. Muscle Res. Cell Motil.* 14:288–291.
2. Kargacin, G. J. 1994. Calcium signaling in restricted diffusion spaces. *Biophys. J.* 67:262–272.
3. Langer, G. A., and A. Peskoff. 1996. Calcium concentration and movement in the diadic cleft space of the cardiac ventricular cell. *Biophys. J.* 70:1169–1182.
4. Greenstein, J. L., and R. L. Winslow. 2002. An integrative model of the cardiac ventricular myocyte incorporating local control of Ca2+ release. *Biophys. J.* 83:2918–2945.
5. Sobie, E. A., K. W. Dilly, J. dos Santos Cruz, W. J. Lederer, and M. S. Jafri. 2002. Termination of cardiac Ca(2+) sparks: an investigative mathematical model of calcium-induced calcium release. *Biophys. J.* 83:59–78.
6. Bers, D. M. 2003. Dynamic imaging in living cells: windows into local signaling. *Sci. STKE.* 2003:PE13.
7. Stern, M. D., L. S. Song, H. Cheng, J. S. Sham, H. T. Yang, K. R. Boheler, and E. Rios. 1999. Local control models of cardiac excitation-contraction coupling. A possible role for allosteric interactions between ryanodine receptors. *J. Gen. Physiol.* 113:469–489.
8. Slepchenko, B. M., J. C. Schaff, J. H. Carson, and L. M. Loew. 2002. Computational cell biology: spatiotemporal simulation of cellular events. *Annu. Rev. Biophys. Biomol. Struct.* 31:423–441.
9. Franzini-Armstrong, C., F. Protasi, and V. Ramesh. 1999. Shape, size, and distribution of Ca(2+) release units and couplons in skeletal and cardiac muscles. *Biophys. J.* 77:1528–1539.
10. Fabiato, A. 1985. Time and calcium dependence of activation and inactivation of calcium-induced release of calcium from the sarcoplasmic reticulum of a skinned canine cardiac Purkinje cell. *J. Gen. Physiol.* 85:247–289.
11. Cheng, H., W. J. Lederer, and M. B. Cannell. 1993. Calcium sparks: elementary events underlying excitation-contraction coupling in heart muscle. *Science.* 262:740–744.
12. Lopez-Lopez, J. R., P. S. Shacklock, C. W. Balke, and W. G. Wier. 1995. Local calcium transients triggered by single L-type calcium channel currents in cardiac cells. *Science.* 268:1042–1045.
13. Stern, M. D. 1992. Theory of excitation-contraction coupling in cardiac muscle. *Biophys. J.* 63:497–517.
14. Cannell, M. B., H. Cheng, and W. J. Lederer. 1995. The control of calcium release in heart muscle. *Science.* 268:1045–1049.

15. Niggli, E., and W. J. Lederer. 1990. Voltage-independent calcium release in heart muscle. *Science*. 250:565–568.

16. Guatimosim, S., K. Dilly, L. F. Santana, M. Saleet Jafri, E. A. Sobie, and W. J. Lederer. 2002. Local Ca(2+) signaling and EC coupling in heart: Ca(2+) sparks and the regulation of the [Ca(2+)](i) transient. *J. Mol. Cell. Cardiol.* 34:941–950.

17. Schaper, J., R. Froede, S. Hein, A. Buck, H. Hashizume, B. Speiser, A. Friedl, and N. Bleese. 1991. Impairment of the myocardial ultrastructure and changes of the cytoskeleton in dilated cardiomyopathy. *Circulation*. 83:504–514.

18. He, J., M. W. Conklin, J. D. Foell, M. R. Wolff, R. A. Haworth, R. Coronado, and T. J. Kamp. 2001. Reduction in density of transverse tubules and L-type Ca(2+) channels in canine tachycardia-induced heart failure. *Cardiovasc. Res.* 49:298–307.

19. Franzini-Armstrong, C. 1991. Simultaneous maturation of transverse tubules and sarcoplasmic reticulum during muscle differentiation in the mouse. *Dev. Biol.* 146:353–363.

20. Kamp, T. J., and J. W. Hell. 2000. Regulation of cardiac L-type calcium channels by protein kinase A and protein kinase C. *Circ. Res.* 87: 1095–1102.

21. Davare, M. A., V. Avdonin, D. D. Hall, E. M. Peden, A. Burette, R. J. Weinberg, M. C. Horne, T. Hoshi, and J. W. Hell. 2001. A beta2 adrenergic receptor signaling complex assembled with the Ca2+ channel Cav1.2. *Science*. 293:98–101.

22. Reiken, S., M. Gaburjakova, S. Guatimosim, A. M. Gomez, J. D'Armiento, D. Burkhoff, J. Wang, G. Vassort, W. J. Lederer, and A. R. Marks. 2003. Protein kinase A phosphorylation of the cardiac calcium release channel (ryanodine receptor) in normal and failing hearts. Role of phosphatases and response to isoproterenol. *J. Biol. Chem.* 278:444–453.

23. Uehara, A., M. Yasukochi, R. Mejia-Alvarez, M. Fill, and I. Imanaga. 2002. Gating kinetics and ligand sensitivity modified by phosphorylation of cardiac ryanodine receptors. *Pflugers Arch.* 444: 202–212.

24. Schroder, F., and S. Herzig. 1999. Effects of beta2-adrenergic stimulation on single-channel gating of rat cardiac L-type Ca2+ channels. *Am. J. Physiol.* 276:H834–H843.

25. Rice, J. J., M. S. Jafri, and R. L. Winslow. 1999. Modeling gain and gradedness of Ca2+ release in the functional unit of the cardiac diadic space. *Biophys. J.* 77:1871–1884.

26. Cannell, M. B., and C. Soeller. 1997. Numerical analysis of ryanodine receptor activation by L-type channel activity in the cardiac muscle diad. *Biophys. J.* 73:112–122.

27. Soeller, C., and M. B. Cannell. 1997. Numerical simulation of local calcium movements during L-type calcium channel gating in the cardiac diad. *Biophys. J.* 73:97–111.

28. Shen, J. X., S. Wang, L. S. Song, T. Han, and H. Cheng. 2004. Polymorphism of Ca2+ sparks evoked from in-focus Ca2+ release units in cardiac myocytes. *Biophys. J.* 86:182–190.

29. Wang, S. Q., M. D. Stern, E. Rios, and H. Cheng. 2004. The quantal nature of Ca2+ sparks and in situ operation of the ryanodine receptor array in cardiac cells. *Proc. Natl. Acad. Sci. USA*. 101:3979–3984.

30. Rios, E., and M. D. Stern. 1997. Calcium in close quarters: microdomain feedback in excitation-contraction coupling and other cell biological phenomena. *Annu. Rev. Biophys. Biomol. Struct.* 26: 47–82.

31. Cannell, M. B., H. Cheng, and W. J. Lederer. 1994. Spatial non-uniformities in [Ca2+]i during excitation-contraction coupling in cardiac myocytes. *Biophys. J.* 67:1942–1956.

32. Stern, M. D., G. Pizarro, and E. Rios. 1997. Local control model of excitation-contraction coupling in skeletal muscle. *J. Gen. Physiol.* 110:415–440.

33. Tijskens, P., G. Meissner, and C. Franzini-Armstrong. 2003. Location of ryanodine and dihydropyridine receptors in frog myocardium. *Biophys. J.* 84:1079–1092.

34. Scriven, D. R., A. Klimek, K. L. Lee, and E. D. Moore. 2002. The molecular architecture of calcium microdomains in rat cardiomyocytes. *Ann. N. Y. Acad. Sci.* 976:488–499.

35. Sedarat, F., L. Xu, E. D. Moore, and G. F. Tibbits. 2000. Colocalization of dihydropyridine and ryanodine receptors in neonate rabbit heart using confocal microscopy. *Am. J. Physiol. Heart Circ. Physiol.* 279:H202–H209.

36. Lohn, M., M. Furstenau, V. Sagach, M. Elger, W. Schulze, F. C. Luft, H. Haller, and M. Gollasch. 2000. Ignition of calcium sparks in arterial and cardiac muscle through caveolae. *Circ. Res.* 87:1034–1039.

37. Wang, S. Q., L. S. Song, E. G. Lakatta, and H. Cheng. 2001. Ca2+ signalling between single L-type Ca2+ channels and ryanodine receptors in heart cells. *Nature*. 410:592–596.

38. Walsh, K. B., and G. E. Parks. 2002. Changes in cardiac myocyte morphology alter the properties of voltage-gated ion channels. *Cardiovasc. Res.* 55:64–75.

39. Gomez, A. M., S. Guatimosim, K. W. Dilly, G. Vassort, and W. J. Lederer. 2001. Heart failure after myocardial infarction: altered excitation-contraction coupling. *Circulation*. 104:688–693.

40. Gomez, A. M., H. H. Valdivia, H. Cheng, M. R. Lederer, L. F. Santana, M. B. Cannell, S. A. McCune, R. A. Altschuld, and W. J. Lederer. 1997. Defective excitation-contraction coupling in experimental cardiac hypertrophy and heart failure. *Science*. 276:800–806.

41. Takekura, H., and C. Franzini-Armstrong. 2002. The structure of Ca(2+) release units in arthropod body muscle indicates an indirect mechanism for excitation-contraction coupling. *Biophys. J.* 83:2742–2753.

42. Wibo, M., G. Bravo, and T. Godfraind. 1991. Postnatal maturation of excitation-contraction coupling in rat ventricle in relation to the subcellular localization and surface density of 1,4-dihydropyridine and ryanodine receptors. *Circ. Res.* 68:662–673.

43. Schroder, F., R. Handrock, D. J. Beuckelmann, S. Hirt, R. Hullin, L. Priebe, R. H. Schwinger, J. Weil, and S. Herzig. 1998. Increased availability and open probability of single L-type calcium channels from failing compared with nonfailing human ventricle. *Circulation*. 98:969–976.

44. Findlay, I. 2002. β-Adrenergic stimulation modulates Ca2+- and voltage-dependent inactivation of L-type Ca2+ channel currents in guinea-pig ventricular myocytes. *J. Physiol.* 541:741–751.

45. Johnson, J. D., C. Snyder, M. Walsh, and M. Flynn. 1996. Effects of myosin light Chain kinase and peptides on Ca exchange with the N- and C-terminal Ca. Binding sites of calmodulin. *J. Biol. Chem.* 271:761–767.

46. Hadley, R. W., and W. J. Lederer. 1991. Ca2+ and voltage inactivate Ca2+ channels in guinea-pig ventricular myocytes through independent mechanisms. *J. Physiol.* 444:257–268.

47. Lee, K. S., E. Marban, and R. W. Tsien. 1985. Inactivation of calcium channels in mammalian heart cells: joint dependence on membrane potential and intracellular calcium. *J. Physiol.* 364:395–411.

48. Peterson, B. Z., C. D. De Maria, J. P. Adelman, and D. T. Yue. 1999. Calmodulin is the Ca^{2+} sensor for Ca^{2+}-dependent inactivation of L-type calcium channels. *Neuron*. 22:549–58.

49. Saftenku, E., A. J. Williams, and R. Sitsapesan. 2001. Markovian models of low and high activity levels of cardiac ryanodine receptors. *Biophys. J.* 80:2727–2741.

50. Mejia-Alvarez, R., C. Kettlun, E. Rios, M. Stern, and M. Fill. 1999. Unitary Ca2+ current through cardiac ryanodine receptor channels under quasi-physiological ionic conditions. *J. Gen. Physiol.* 113: 177–186.

51. Fill, M., and J. A. Copello. 2002. Ryanodine receptor calcium release channels. *Physiol. Rev.* 82:893–922.

52. Hinch, R. 2004. A mathematical analysis of the generation and termination of calcium sparks. *Biophys. J.* 86:1293–1307.

53. Sarkozi, S., C. Szegedi, P. Szentesi, L. Csernoch, L. Kovacs, and I. Jona. 2000. Regulation of the rat sarcoplasmic reticulum calcium release channel by calcium. *J. Muscle Res. Cell Motil.* 21:131–138.

54. Hain, J., H. Onoue, M. Mayrleitner, S. Fleischer, and H. Schindler. 1995. Phosphorylation modulates the function of the calcium release channel of sarcoplasmic reticulum from cardiac muscle. *J. Biol. Chem.* 270:2074–2081.

55. Smith, G. D., J. E. Keizer, M. D. Stern, W. J. Lederer, and H. Cheng. 1998. A simple numerical model of calcium spark formation and detection in cardiac myocytes. *Biophys. J.* 75:15–32.

56. Franks, K. M., T. M. Bartol, Jr., and T. J. Sejnowski. 2002. A Monte Carlo model reveals independent signaling at central glutamatergic synapses. *Biophys. J.* 83:2333–2348.

57. Faber, G. M., and Y. Rudy. 2000. Action potential and contractility changes in [Na(+)](i) overloaded cardiac myocytes: a simulation study. *Biophys. J.* 78:2392–2404.

58. Alseikhan, B. A., C. D. DeMaria, H. M. Colecraft, and D. T. Yue. 2002. Engineered calmodulins reveal the unexpected eminence of Ca2+ channel inactivation in controlling heart excitation. *Proc. Natl. Acad. Sci. USA.* 99:17185–17190.

59. Bers, D. M. 2002. Cardiac excitation-contraction coupling. *Nature.* 415: 198–205.

60. Izu, L. T., W. G. Wier, and C. W. Balke. 2001. Evolution of cardiac calcium waves from stochastic calcium sparks. *Biophys. J.* 80:103–120.

61. Bers, D. M. 2001. Excitation-contraction coupling and cardiac contractile force. Kluwer Academic Publishers, Dordrecht/Boston:.

62. Cannell, M. B., and C. Soeller. 1999. Mechanisms underlying calcium sparks in cardiac muscle. *J. Gen. Physiol.* 113:373–376.

63. Jafri, M. S., J. J. Rice, and R. L. Winslow. 1998. Cardiac Ca2+ dynamics: the roles of ryanodine receptor adaptation and sarcoplasmic reticulum load. *Biophys. J.* 74:1149–1168.

64. Fill, M., and R. Coronado. 1988. Ryanodine receptor channel of sarcoplasmic reticulum. *Trends Neurosci.* 11:453–457.

65. Smith, J. S., T. Imagawa, J. Ma, M. Fill, K. P. Campbell, and R. Coronado. 1988. Purified ryanodine receptor from rabbit skeletal muscle is the calcium-release channel of sarcoplasmic reticulum. *J. Gen. Physiol.* 92:1–26.

66. Marx, S. O., J. Gaburjakova, M. Gaburjakova, C. Henrikson, K. Ondrias, and A. R. Marks. 2001. Coupled gating between cardiac calcium release channels (ryanodine receptors). *Circ. Res.* 88:1151–1158.

67. Timerman, A. P., H. Onoue, H. B. Xin, S. Barg, J. Copello, G. Wiederrecht, and S. Fleischer. 1996. Selective binding of FKBP12.6 by the cardiac ryanodine receptor. *J. Biol. Chem.* 271:20385–20391.

68. Sharma, M. R., P. Penczek, R. Grassucci, H. B. Xin, S. Fleischer, and T. Wagenknecht. 1998. Cryoelectron microscopy and image analysis of the cardiac ryanodine receptor. *J. Biol. Chem.* 273:18429–18434.

69. Brette, F., and C. Orchard. 2003. T-tubule function in mammalian cardiac myocytes. *Circ. Res.* 92:1182–1192.